Engineering Failure Analysis 151 (2023) 107417

Contents lists available at ScienceDirect

Engineering Failure Analysis

journal homepage: www.elsevier.com/locate/engfailanal

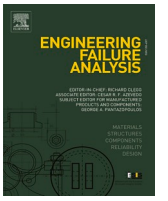

A macroblock 2D finite element model for assessing the roots of failure of Huaca de la Luna's main pyramid (Peru) under seismic action

Cristiana Riccio [a], Anna Remus [b], Selman Tezcan [b,c], Luis C. Silva [a], Gabriele Milani [a], Renato Perucchio [b,*]

[a] *Department of Architecture, Built Environment and Construction Engineering, Politecnico di Milano, Campus Leonardo – Piazza Leonardo Da Vinci 32, 20133, Italy*

[b] *Department of Mechanical Engineering, Hajim School of Engineering and Applied Sciences, University of Rochester, Rochester 14627, NY, United States*

[c] *Department of Mechanical Engineering, Bilecik Şeyh Edebali University, 11230 Bilecik, Turkey*

ARTICLE INFO

Keywords:
Civil engineering
Historic masonry building
Adobe masonry
Finite element method
Nonlinear static analyses
Nonlinear dynamic analyses
Overload brittle fracture
Seismic vulnerability

ABSTRACT

This study contributes to the seismic structural failure analysis of the main pyramid of the archaeological complex Huaca de la Luna, Peru. Built with millions of adobe bricks by the Moche civilization (200–850C.E.), the monument is one of the largest adobe structures in the world. The monument shows signs of severe natural and anthropogenic damage due to its position along the Pacific Ring of Fire and extensive looting since Spanish colonial times. The pyramid was built as a succession of taller and larger platforms, each formed by erecting adjacent but disconnected vertical piers made of adobe masonry. A multiscale 2D nonlinear finite element (FE) model is introduced for assessing the contribution of this pier architecture to the structural response of the pyramid. The time-evolution of elastic strain and plastic dissipation energies is used to quantitatively track structural failure. The instant of structural collapse and attendant lateral capacity can be extracted from the point at which these energies match. Critical regions of a representative cross-section are modelled with individual piers represented by macroblocks and separated by frictional interfaces. A continuous description is adopted for the remaining part of the model. A nonlinear, two-dimensional (2D) plane strain analysis is conducted in Abaqus/CAE Explicit using concrete damaged plasticity and Mohr-Coulomb formulations for adobe construction and soft soil, respectively. A two-stage assessment procedure begins with a quasi-static analysis to predict the stress state due to gravitational load. A dynamic analysis follows to identify lateral capacity and failure mechanisms triggered by monotonically increasing ground acceleration. The development of local damage conditions up to structural collapse is visualized by the nucleation and propagation of maximum principal plastic strains throughout the model. A sensitivity analysis was conducted to evaluate the effect on lateral capacity of the contact friction coefficient between macroblocks and the number of macroblocks used to discretize the critical area. Introducing macroblocks to the model produces lateral capacities that are lower than analogous, purely-continuum models. These results are shown to be critically affected by the frictional coefficient

* Corresponding author.
E-mail addresses: cristiana.riccio@mail.polimi.it (C. Riccio), aremus2@ur.rochester.edu (A. Remus), stezcan@ur.rochester.edu, selman.tezcan@bilecik.edu.tr (S. Tezcan), luiscarlos.martinsdasilva@polimi.it (L.C. Silva), gabriele.milani@polimi.it (G. Milani), rlp@me.rochester.edu (R. Perucchio).

https://doi.org/10.1016/j.engfailanal.2023.107417
Received 22 March 2023; Received in revised form 20 May 2023; Accepted 16 June 2023
Available online 17 June 2023

that governs contact between the macroblocks. The results of this study offer critical insights on the consolidation strategy for the northwest corner of the pyramid and may find application to similarly-built historical earthen structures in northern Peru.

1. Introduction

Heritage buildings' historic and cultural value contributes to societal identity and continuity [1]. Aiming at the safeguard of the heritage buildings' significance, the International Council on Monuments and Sites (ICOMOS) [2] call for conservation principles and recommendations that are based on centuries of ideological evolution [3,4]. The present study contributes to the structural assessment of the main pyramid of Huaca de la Luna, one of the most representative archaeological sites of the pre-Columbian Moche society in Peru [5]. This impressive archaeologic complex dates to the period 200C.E. to 850C.E and provides a testament to massive earthen architecture and structural techniques of the past. It is recognized as world heritage by the World Monuments Fund [6]. Built with adobe bricks in a seismically active area and exposed to extensive looting during colonial times, the monument shows signs of severe natural and anthropogenic damage. A comprehensive structural assessment is an essential requirement for the selection of appropriate preservation and intervention strategies [7–10]. Moreover, unreinforced masonry (URM) and adobe buildings present a high seismic vulnerability [11,12] due to: (i) a low tensile strength and thus limited out-of-plane capacity; (ii) reduced capacity to dissipate energy; (iii) lack of proper connections between structural elements [13,14] and (iv) deterioration of materials over time [15].

The structural assessment of heritage buildings is often a challenge. Sound knowledge of the structural and material features lack in most cases [16] and the mechanical response of masonry is rather complex [17,18], with a generally relevant uncertainty associated with the monuments' loading paths. This uncertainty can be reasonably addressed through sensitivity analysis [19]. Scientifically based intervention is required for correct evaluation, thus the methodology should be incremental and include studies such as an historical literature review, inspections, monitoring actions, and structural analysis [20,21], as noted from ICOMOS principles [22]. In the evaluation of structural safety, numerical modelling is a valuable contribution to assess the structural response of historical buildings. To this end, the literature has been enriched with the development of analysis methods for masonry structures [23,24]. For instance, the use of rational (or analytical) approaches is practical and provides fast solutions, whereas graphical methods are difficult to apply in structures with complex geometries. Limit analysis is useful to estimate the structural load capacity, yet still requires an expert-based decision to ascertain the potential collapse mechanisms [17,25,26].

More advanced models, such as the Finite Element Method (FEM) [27–30] and the Discrete Element Method (DEM) [31–37] are largely used. DEM is suited for masonries with both dry and mortared joints, but it requires a full representation of the masonry units' arrangement [34]. FEM models generally rely either on a micro- or macro-modelling approach. Both can be successfully performed in the software Abaqus/CAE [38], which has been used successfully for masonry analysis [12,25,39] and is applied presently. In the former, the masonry components (units, mortar, and unit/mortar interface) are discretizeds individually, leading to a large number of degrees of freedom and consequently to higher processing times [40,41]. In the latter, masonry is modelled as a continuum and assumes a homogeneous material that can be isotropic or anisotropic [42]. This modelling approach is generally preferred in the analysis of large structures, as shown in [43–46]. Nonetheless, the mechanical deformation and failure of masonry is inherently a multi-scale phenomenon, for which the observed macroscopic behaviour of the material is governed by processes that occurs at finer scales [47]. The connection between different length scales is well demonstrated but representing masonry at finer levels (micro- or mesoscale) may be computationally prohibitive and lack practical sense. In such a context, the so-called multi-scale or coupled methods have recently been employed to masonry structures. Although first works date back to 1970 [48,49], their present use may increase the effectiveness of FE models by guaranteeing an accurate description in regions were fracture occurs [50–53].

In such a context, the main contribution of the present study is to provide a rational-based and practical strategy for the structural assessment of Huaca de la Luna's main pyramid. This monumental structure is the result of a succession of construction stages. Each new stage encapsulates in its interior all preceding constructions, resulting in an increasingly large and tall structure. Each platform was formed by erecting adjacent but disconnected vertical piers made of well-textured adobe masonry. In the present study, a multiscale 2D macro-FE model is introduced for assessing the contribution of this pier architecture to the static and dynamic response of the entire pyramid. Critical regions previously determined in [54,55,57] are modelled using individual piers explicitly represented by macroblocks and separated by frictional interfaces. A continuum is adopted for the remaining part of the cross-section. The same material macro-modelling approach is used to represent adobe in the macroblocks and the continuum. Such a modelling assumption may increase the accuracy of the representation of failure and allows us to better evaluate the sensitivity of the results with respect to the uncertainty of geometrical and material properties. Additionally, an energy-based approach is used to determine collapse conditions when performing a nonlinear static or dynamic analysis. Similar energy-based approaches have been explored to identify the sequential failure of macro-elements of structures, such as [14,58], or to track the existence of fracture in masonry structures related to localized cracking [59].

This study intends to provide an important basis for further structural-related studies on monumental and historic buildings, especially in Peru where several alike adobe masonry constructions are found along the coast. The paper is organized into the following sections: Section 2 describes the main structural features and present state of damage at Huaca de la Luna; Section 3 describes the FE model's geometry and macroblocks, mesh, and material characterization; Section 4 explains the two-stage analysis procedure and the energy-based approach used to determine lateral capacity; Section 5 presents the results of the sensitivity analysis; and Section 6 offers conclusions and identifies directions for future work.

2. Huaca de la Luna

The monumental complex of Huaca de la Luna is part of the Huacas de Moche archaeological site located near the modern city of Trujillo in north coastal Peru. Huaca de la Luna was erected on the lower slopes of the Cerro Blanco – Fig. 1(a) – as part of a sprawling urban centre considered to be a ceremonial centre of the Moche culture. The complex has a surface area that covers approximately 30,000 square meters and reaches a height of approximately 28 m, making it one of the largest adobe structures in the world. After the decline of the Moche culture, circa 850C.E., the complex was naturally buried under aeolian sand deposits, which reduced exposure to seismic loading demands during possible historical earthquakes in that region of Peru. The archaeological works that started in the beginning of the 90 s has systematically unearthed and exposed the majority of the Huaca de la Luna complex [6].

The complex is constructed using adobe masonry. It is estimated that more than 50 million bricks have been used for its construction and are from various sources, i.e. some adobes are of granular yellow sediments from deserts and some contain organic matter [61]. Piers constitute a unique construction feature of the Huaca. They are large brick columns of non-uniform height, width, and depth, arranged side-by-side to form platforms and walls, Fig. 2. The discontinuities between adjacent piers are clearly visible in the figure. It is noteworthy that a significant number of bricks have "maker's marks" imprinted and similar symbols appear often within the same pier, suggesting that coordinated but separate social units worked together to construct the monument [62].

The study focuses on the main stepped pyramid at the centre of the complex. Built on the slopes of the Cerro Blanco Mountain, the pyramid is supported on the east side by sloping bedrock and is built directly on layers of soft soil on the west side. The complex belongs to the peak of Moche development and archaeologists conclude it had a ceremonial role based on its internal organization, iconographic murals depicting gods, sacred animals, and other motifs, and construction technique [6]. Six overlapping construction levels (A, B, C, D, E, and F) have been identified within the main pyramid (Fig. 3). The layers A-E were added by filling negative architectural space with the previously mentioned "piers" of adobe blocks, adjacent columns separated by construction joints [6,62]. The most accepted justification for construction layers is rooted in the idea that it was part of a renewal of power, corresponding to the start of a new era of influence, i.e. ruler or priest of some kind [6].

The most striking and famous feature of Huaca de la Luna is the main pyramid's stunning North Façade which faces the largest and most public plaza (Fig. 3a). The polychrome reliefs of the North Façade mark the public ceremonial importance of the temple.

Archaeological excavation started in the early 1990 s and was followed by surveys and studies that produced quantitative measurements and revealing pictures of the earthen structure's most dominating features. The state of preservation at the complex was remarkable due to the protective layer of aeolian sand (Fig. 4) that covered it. However, its removal exposed the structure to the direct consequence of seismic, climactic, and anthropogenic hazards.

The present state of damage has been extensively documented in archaeological reports and in existing structural investigations [6,60,64,65]. The pyramid shows signs of extensive anthropogenic and natural damage, primarily in the northwest corner north and west façade – Fig. 1(b). A large excavation, attributed to treasure hunting during colonial time, cuts deeply in the north façade (Fig. 5). Structural damage is mainly present in the NW sector of the pyramid including the substantial collapse of the NW corner and large cracks in the upper areas, which penetrate deeply in the structural system (Fig. 5).

The pyramid has been the ongoing objective of a multidisciplinary study focused on determining the structural behaviour of its massive core and the built-up areas on the top of the pyramid under static and dynamic conditions. This includes laser-scan survey and 3D reconstruction of the pyramid [60,66], mechanical characterization of adobe brick and mud mortar [67,68] and geotechnical and geophysical exploration of the foundation soils along the northern façade [67,69].

Initial structural research investigated the relationship between the observed damage and the soft soil support under static conditions using a simplified plane strain nonlinear FE model derived from the geometry and the ground level of the north façade [64]. Subsequent research focused on the west side of the pyramid to capture the effect of the original ground level (located 5.5 m below the north side) on the dynamic response. Most recently, a sensitivity analysis of the static and dynamic response to (a) variations in the pyramid's stepped west side profile, (b) underlying soft soil and bedrock configuration, and (c) tensile strength of adobe material was performed on 2- and 3D nonlinear FE models [54,55,57]. In each case analysed, the dynamic response was evaluated by applying

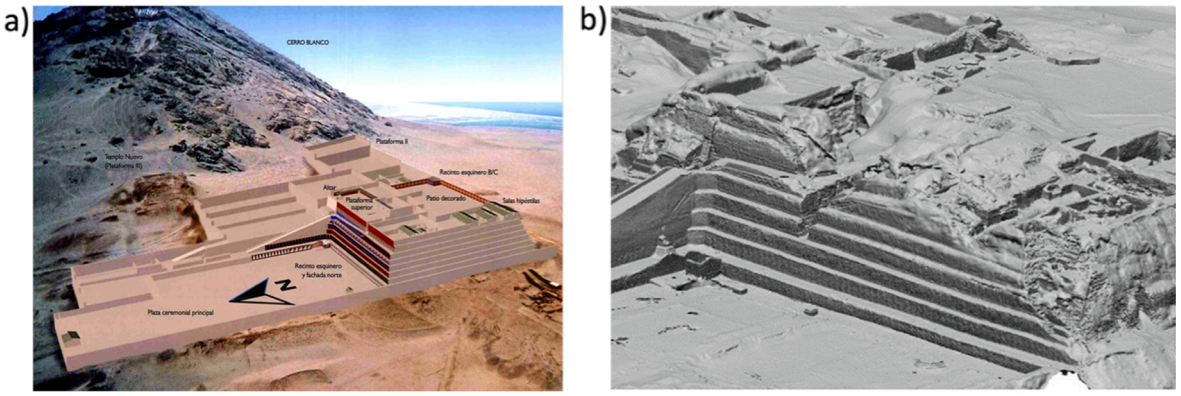

Fig. 1. Huaca de la Luna: (a) 3D CAD reconstruction, and (b) laser scanning of the main pyramid's north façade [60].

Fig. 2. Main pyramid: divisions between “piers” of adobe bricks.

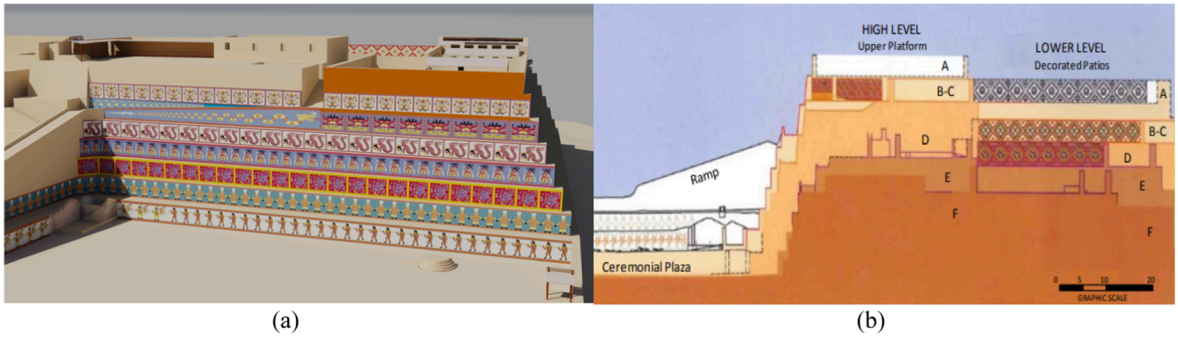

Fig. 3. Main pyramid of Huaca de la Luna: (a) rendering of the North Façade and (b) North-South section with distinct construction stages [6].

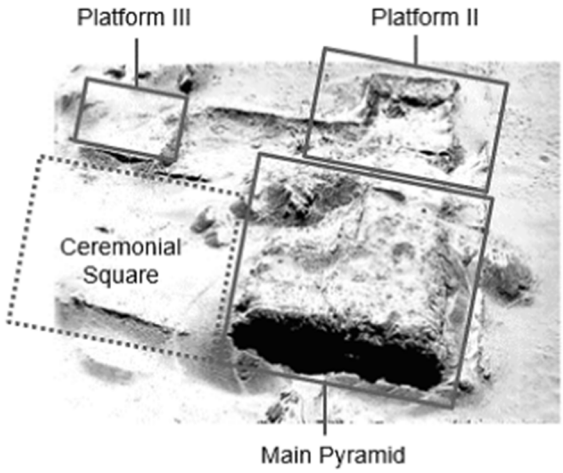

Fig. 4. Aerial photograph that captures the aeolian sand drifts that covered the monument before excavation of the site started in 1991 [63].

lateral ground accelerations that led to the structural collapse of the stepped (west) side of 2D models and of the NW corner of 3D models. Based on a continuous description of the adobe masonry using a material macro-model, these studies demonstrated the seismic fragility of the northwest corner. Lateral capacity for 2D models was found to range between 0.135 g and 0.340 g. The combination of the steepest bedrock angle and lowest adobe tensile strength yielded critical conditions. Results from [54] suggested the need for a refined model, which would account for the discontinuities between piers of the adobe structure and the frictional interaction between them.

Fig. 5. Extant damage: (a) colonial "looter's cut" on the North Façade and (b) collapse of the northwest corner.

3. Characterization of 2D finite element models

A two-dimensional (2D) finite element (FE) model of a representative internal cross-section of Huaca de la Luna's main pyramid is presented. Given the complexity of the construction system, the first step toward a successful model in 3D is preliminary analysis in 2D. The plane strain model allows an extensive preliminary sensitivity analysis of contact friction parameters and macroblock configurations. As block stereotomy can be expected to influence structural response [70], subsequent 3D analysis will be used to address the effect introduced by horizontal and vertical staggering of the construction piers. Additionally, choosing to perform preliminary research in 2D offers the additional benefit of allowing comparison with previous research [55,57]. The required tasks addressed next include the modelling of the geometry, the mechanical behaviour of materials, the FE mesh discretization and the assumed boundary and loading conditions.

3.1. Geometry and macroblocks

The EW cross section of the main pyramid is based on previous studies [54,55] and is adapted for 2D plane strain nonlinear FE analysis in Abaqus/CAE Explicit [38]. The chosen cross-section has a total length of 122.80 m, where 82.80 m corresponds to the width of the pyramid itself and 40 m corresponds to the width of the adjacent Plaza 2b (Fig. 6a). At its greatest height, the monument reaches 28.6 m from west ground level. The section model was selected from a sensitivity analysis of potential foundation conditions and west façade configurations as an intermediate version appropriate for preliminary investigation of macroblocks.

In order to overcome the limitations identified in existing numerical studies that are based on a continuum-like approach [54,55,57], an explicit modelling of adobe piers is produced using macroblocks. The systematic 2D static and dynamic modelling in those studies have identified critical damage development in the western portion of the cross section, culminating with partial or total collapse of the stepped façade. This so-called active region corresponds – within the approximation intrinsic to a 2D plane strain model – to the west façade including the damaged NW corner of the actual pyramid. Thus, to effectively model how piers affect damage development and collapse mechanisms, macroblocks are distributed from the west façade to the interior of the cross section. Five cross sectional configurations of increasingly deeper macroblock distribution are considered, with the total number of macroblocks ranging from 37 to 103 (Fig. 6b-f). The remaining part of the cross section, shown in grey, is modelled as a single continuum. This optimizes the computation processing time of the analysis, especially relevant in the analysis of large-scale structures [71].

Furthermore, to avoid unnecessary complexities in this preliminary attempt at modelling piers, the geometry of the pier structure is simplified. Each of the nine steps of the reconstructed west façade [54,55,57] is assumed to correspond to one single layer of identical rectangular macroblocks. The height of the macroblocks ranges between 2.75 m at the bottom layer and 3.16 m at the top. Based on an estimate of observable piers, the width of the macroblocks varies according to the layer with 4.3 m at the bottom layer and 3.5 m at the top.

The foundation soil is also modelled with the goal of reproducing the soil-structure interaction. A single and homogenous layer of soil (medium sand) has been modelled, which starts from the hypothetical position of the bedrock. It has a total extension of 150 m from the bedrock (Fig. 6a). This length was considered necessary to avoid a possible dependence between the provided boundary condition and the actual movement of the soil when subjected to vertical and lateral loading.

3.2. Finite element mesh

The FE model was discretized in Abaqus/CAE Explicit following a mapped type of mesh using linear interpolation FEs. Quadrilateral elements (CPE4R) are predominant; a limited of triangular FEs (CPE3) are found mostly in corner regions. Mesh refinement was increased in the vicinity of the active region in which the macro-elements are positioned. The FE mesh characteristic length varies as given in Fig. 7(a) for Model 3. In particular, the FEs that describe the macroblocks have an approximate size of 0.75 m, and the

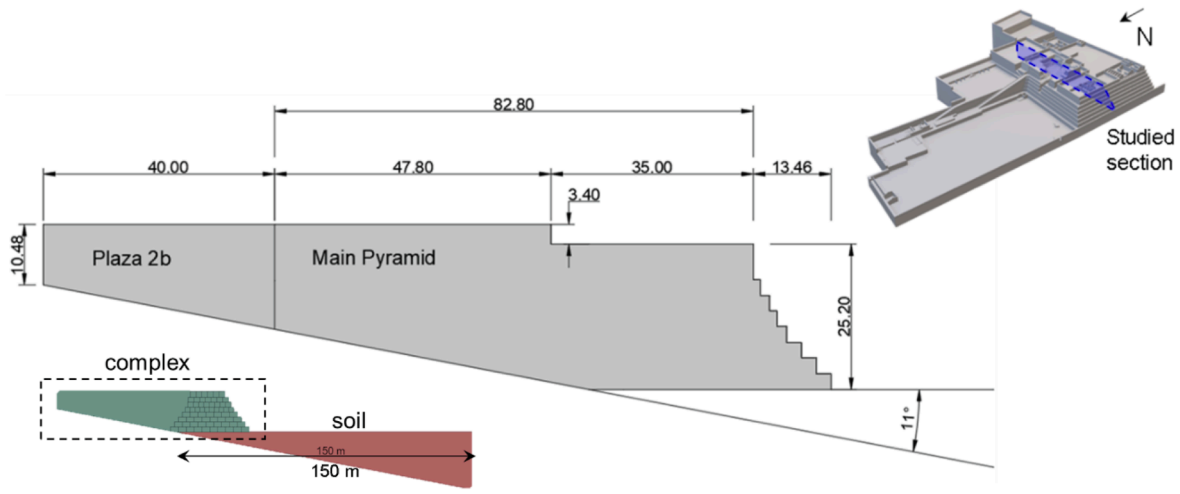

(a) geometry of the selected east-west cross-section

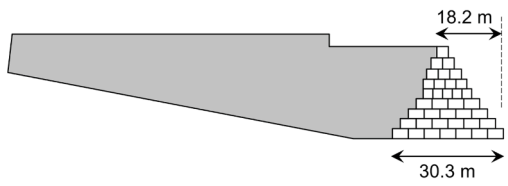

(b) model 1: N=37

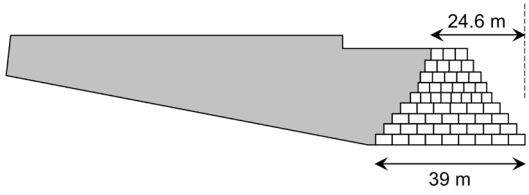

(c) model 2: N=56

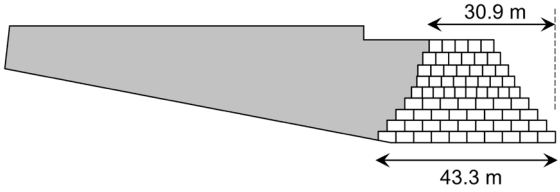

(d) model 3 (reference): N=70

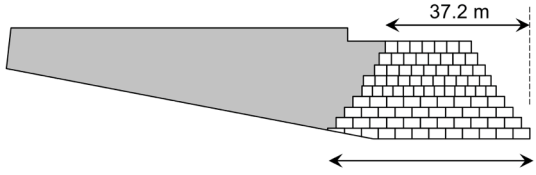

(e) model 4: N=90

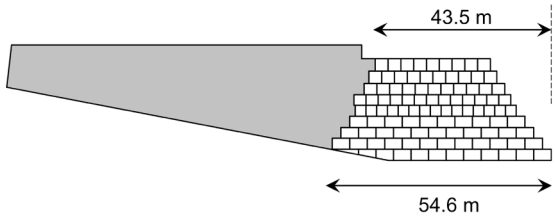

(f) model 5: N=103

Fig. 6. Geometry: (a) dimensions and location of cross-section and (b-f) macroblock configurations for the sensitivity analysis (in (b) through (f) the soil is omitted for clarity).

remaining part of the pyramid wall is defined by a coarse mesh with 1.5 m of size. For the soil that supports the active region and is extended to the west (right), the element size increases progressively from 0.75 m at the base of the monument to 1.5 m at the westernmost edge. The final FE Model 3 has a total of 5416 CPE4R and 118 CPE3 FEs that lead to 12,898 degrees of freedom. The boundary conditions applied to the numerical model are presented in Fig. 9. Pinned supports are assumed at the base to simulate the full supporting effect provided by the bedrock below the sand layer. At the westernmost (right) side of the foundation soil, rollers restrain motion in the horizontal x-direction and simulate soil beyond the scope of the model. This support is maintained under gravitational loading only. When the lateral load is applied, rollers are removed and replaced with horizontal acceleration, Fig. 9 (b). The bedrock level support is also modified to include horizontal acceleration. Details are provided again in Section 4, which is devoted

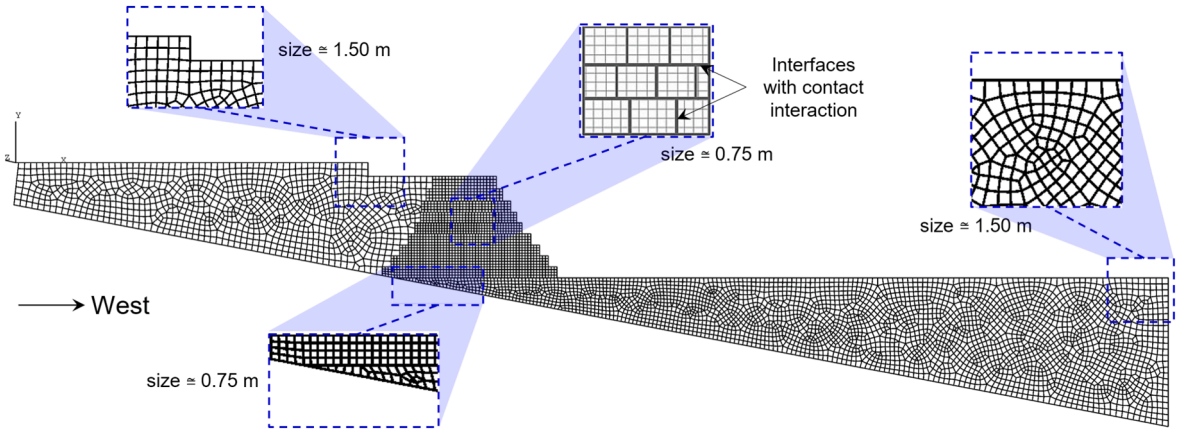

Fig. 7. FE mesh for the reference configuration (model 3 in Fig. 6d).

to the results of the numerical structural analyses.

3.3. *Material and interface contact properties*

The material properties assumed for both the adobe masonry and the soil of the foundation are provided, together with the contact properties for the interfaces between macro-elements. The assumptions made are supported by existing mechanical characterization tests [64,67,68]. Adobe masonry has been modelled as a continuum and defined as a homogeneous and isotropic material. These assumptions are compatible with both CDP and total strain crack (TSC) formulations [72,73]. For the purposes of comparison with previous research [55,57], the material behaviour of adobe is reproduced according to the CDP model available in Abaqus/CAE Explicit [38]. Abaqus/CAE is preferred due to its immediate output of energy results and the possibility of modelling extreme deformations with the explicit formulation, which could otherwise cause numerical failure due to stiffness matrix singularity in the implicit FE formulation. This plasticity model is suitable for quasi-brittle materials in general [28,74–77] and assumes an elastic isotropic behaviour. The inability of reproducing material orthotropy does not constitute a contentious issue for adobe masonries. Adobe can be well approximated as an elastic isotropic material [78], given that the orthotropy could be induced by the geometrical arrangement of the units. This demonstrates the importance of an explicit discretization of the blocks and the relevance of considering the five different models.

The CDP formulation can be used with different strength values and post-peak behaviours for both tension and compression regimes, and it can include a cohesive frictional behaviour for the shear regime. It is extensively used in large masonry structures [12,14,19,28,44,54–57,74] and results indicate that it offers a good compromise between computational time and accuracy. Material response is described in terms of effective stress and strain (or displacement) relationships. The quasi-brittle nature of adobe masonry was represented by an exponential type of softening in tension. In compression, a parabolic type hardening exists being followed by a softening regime. The post-peak responses that serve as input for the CDP model are depicted in Fig. 8 and are based on the data available from previous experimentation [64].

The CDP model assumes a non-associated flow rule given as a Drucker-Prager hyperbolic function and requires the definition of

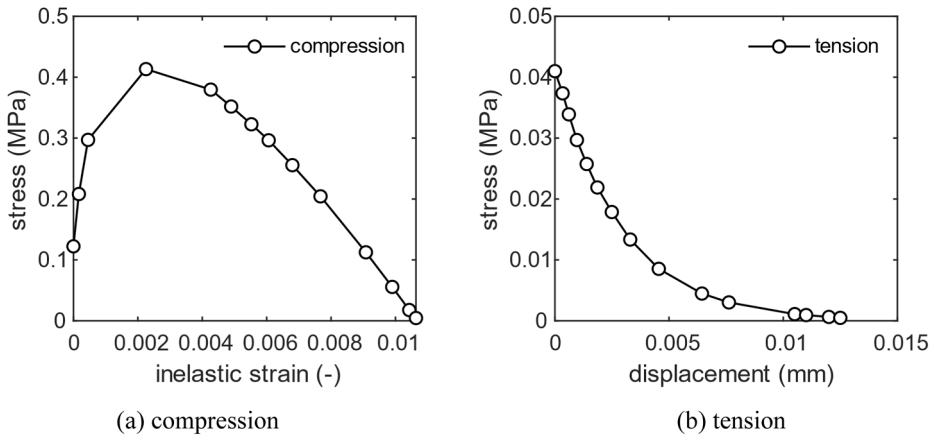

Fig. 8. Postcritical constitutive laws adopted for adobe masonry [64].

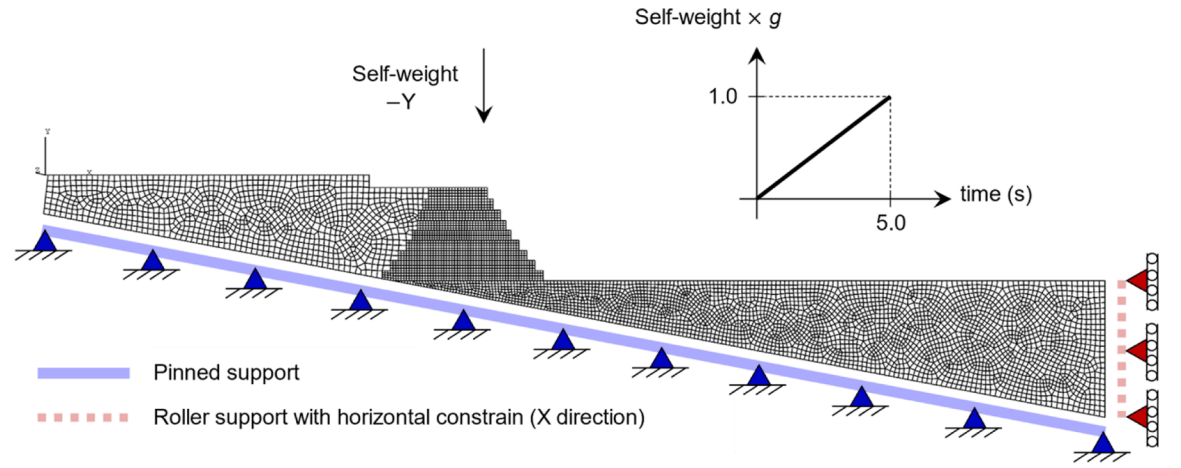

(a) stage 1: self-weight

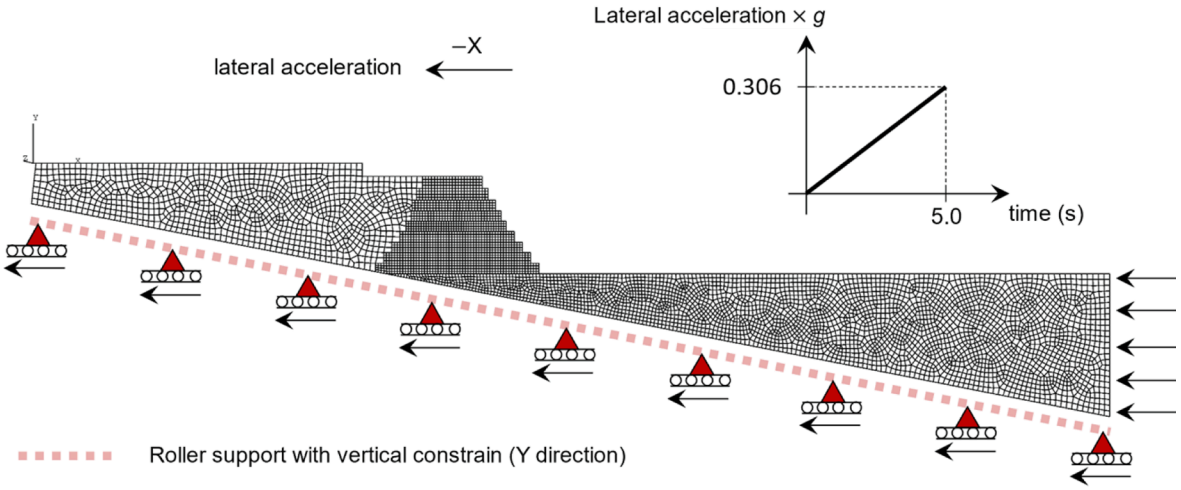

(b) stage 2: lateral earthquake acceleration

Fig. 9. Loading stages for the sequential analysis of the FE model.

several physically-based parameters. The Drucker-Prager strength domain criterion was modified through a parameter $K_c = 2/3$ to approximate it with a Mohr-Coulomb criterion. The eccentricity parameter was assumed as 0.1 [77] and expresses the rate at which the plastic flow potential approaches the Drucker-Prager function for high confining pressure levels. A dilation angle of 18 degrees and a ratio between the bidirectional and unidirectional compressive strengths of masonry of 1.16 [77] were assumed. A low viscosity parameter of 0.0005 – required for numerical stabilization and convergence during the explicit analysis [38] – was adopted and the analyses indicated it is an adequate choice. These parameters are described in Table 1. The reader is referred to [38,76,77] for further details on the implementation of the CDP model.

The behaviour of the soil foundation was simulated through a Mohr-Coulomb law. Soil properties are averaged from data produced via cone penetration tests performed around the perimeter of the monument [64,67,69]. The stratification of soil in the vicinity of structure was approximated as a single layer. The material properties are assumed to be averaged values from the material properties identified for each stratum; they are summarized in Table 2.

Table 1
Material properties adopted in the simulations for the adobe masonry through the CDP model.

Density (kg/m^3)	Elastic modulus (MPa)	Poisson's ratio	Tensile strength (MPa)	Compressive strength (MPa)	Dilation angle (degrees)	Eccentricity	f_{b0}/f_{c0}	K_c	Viscosity
1735	123	0.2	0.0409	0.41	18	0.1	1.16	2/3	0.0005

Finally, the interactions between macroblocks were idealized through Abaqus/CAE Explicit's general contact formulation. Both shear and normal behaviour is defined through a penalty approach [38]. For the shear (tangential) response, the contact is defined by a Coulomb friction model with a friction coefficient μ, whose value is assumed to range from 0.1 to 0.5. For the normal response, a hard contact has been adopted and the inter-penetration between blocks under compression is precluded. Macroblocks are permitted to detach in pure tension.

4. Structural analysis procedure

Numerical simulations are performed to estimate the structural lateral capacity of the Huaca's main pyramid as affected by the macroblock architecture. The study systematically investigates the effect of different macroblocks discretization and of variations of the frictional coefficient between macroblocks on the structure's response.

A two-stage analysis is undertaken. First, a quasi-static analysis is conducted, in which the self-weight is applied with the objective of predicting the existing stress distribution and resulting damage state of the structure. Second, a dynamic analysis follows, in which a monotonically increasing horizontal ground acceleration is applied, with the goal of identifying failure mechanisms and estimating the lateral capacity. The second stage resembles a classical pushover analysis in that it determines the response to a peak lateral ground acceleration, but it does so without applying an arbitrary acceleration distribution directly to the adobe mass. Rather, closely simulating earthquake-induced ground acceleration, it employs the underlying bedrock motion to induce a distribution of lateral inertial forces in the soil and the adobe mass that are coherent with the acceleration transmitted from the boundary to the rest of the deformable domain.

The explicit dynamic FE formulation available in Abaqus/CAE Explicit is preferred over the standard implicit formulation since it allows for large deformations to develop in the nonlinear model without premature failure due to the numerical singularity of the stiffness matrix. CDP models of masonry structures have shown that structural failure conditions can be unambiguously detected before the analysis fails due to numerical problems if the explicit formulation is used [56]. Although generally used to model impact dynamics, the explicit formulation is successfully applied in the present context to produce quasi-static analytical conditions during dead-weight loading. This is achieved by selecting suitably long analytical time intervals for the gradual application of gravitational acceleration. The development of kinetic energy remains negligible as long as static stability is maintained, i.e. less than 5% of the total internal energy, as recommended [38]. Sub-section 4.2 reviews the energy-based approach for structural failure analysis adopted in conjunction with explicit FE modelling.

4.1. Quasi-static and dynamic analysis stages

The two sequential stages are given in Fig. 9. The first concerns the application of self-weight to the entire numerical model as a body force. To this end, gravitational acceleration is applied as a linear ramp growing from 0g to 1g over an interval of 5 s, allowing a slow deformation rate and producing quasi-static conditions within the explicit analytical formulation. During this step, the sloping base of the monument is fully constrained. At the right side, the supporting soil is free to move only vertically; this condition represents the mechanical effect of soil beyond the rightmost boundary.

During the second stage, a lateral acceleration is applied to the model at the boundaries, simulating the effect of ground acceleration. As shown in Fig. 9(b), the previous full constraint of the sloping base is relaxed. Along the bedrock, boundary conditions previously fixed in both horizontal (x) and vertical (y) directions are modified to allow acceleration in the horizontal direction only. Along the vertical boundary at the west side, the nodes that were previously constrained in the horizontal (x) direction only are now accelerated in the -x direction. An equal acceleration is applied to the base and soil boundary. The acceleration increases linearly from 0 g to 0.306 g (3 m/s^2) over a 5 s interval. The upper limit of the acceleration is based on the lateral capacity of the analogous 2D continuum model given in [54,55,57].

The rigid translation of the boundary produces internal inertial forces resulting from the intrinsic deformability of the structure, in contrast to conventional pushover analysis where a displacement or force distribution derived from eigen-frequencies analysis of the linear elastic model is applied to the structure. By applying acceleration to the base of the model, we produce a condition that more realistically represents how seismic load is transmitted to a structure from the ground. In fact, due to the material characteristics, the model reaches nonlinear conditions due to plastic strain distributions at the end of gravitational loading. Thus, the eigen-frequencies analysis and the attendant displacements of force distributions may not lead to a correct application of internal inertial forces acting on the model during the dynamic stage. This problem is completely bypassed but letting the nonlinear model develop the appropriate inertial response under boundary applied accelerations.

The two-stage nonlinear structural analysis is set to finish in 10 s of analytical time, with 5 s of quasi-static loading followed by 5 s of dynamic loading. However, the analysis proper is considered completed at the time of structural failure which takes place before the 10 s limit, for all cases considered in this study. The nonlinear model becomes numerically unstable shortly thereafter, and the analysis

Table 2
Material parameters adopted for the foundation soil assuming a Mohr-Coulomb formulation.

Young's Modulus (MPa)	Poisson's ratio	Density (kg/m^3)	Friction Angle ϕ(deg)	Dilation Angle ψ (deg)	Cohesion (kPa)
57	0.42	2000	43	13	0.010

aborts due to exceedingly large deformations. The definition of what constitutes structural failure in this nonlinear dynamic context is discussed next.

4.2. Energy-based determination of lateral capacity

To determine the enucleation of local damage and its evolution into structural failure under static or dynamic conditions, we apply the energy-based approach previously developed for the static and dynamic assessment of CDP models representing historical structures [54–57,79]. This approach provides a rational strategy to numerically determine the lateral capacity of the pyramid model. The basic postulate is that structural failure of a masonry construction – either due to static or dynamic loading – can be defined as the transition from a stable to an unstable equilibrium condition for either the entire structure or portion(s) of it. In a numerical model, this transition can be identified by a sudden variation of support reactions. Failure also produces the asymptotic growth of kinetic energy, since, in order to fail, the structure must ultimately separate into disconnected elements which move with increasing velocity under the applied forces. In nonlinear FE analyses using CDP material formulations, fracture propagation is represented as a zone of plastic strain growth, which in turn produces plastic dissipation energy. In the limit, for separated elements to move independently, plastic strains – and with them plastic dissipation energy – must grow asymptotically. Thus, in CDP models, the failure growth in kinetic energy is accompanied by the asymptotic growth of plastic dissipation energy.

Under dynamic conditions produced by ground acceleration as applied in the present study, the entire FE model translates with increasing velocity, which, given the large mass involved, produces a fast growth of kinetic energy. In this case, the variation of kinetic energy due to structural failure may not be easily distinguished from the high level of kinetic energy already present in the structure. In these circumstances, failure conditions can still be effectively determined based on a change in support reactions, the asymptotic growth of plastic dissipative energy, or both.

The application of the energy-based approach in the present context is illustrated with the example in Fig. 10. A 5 by 5 m adobe macroblock subjected to gravitational loading and ground acceleration is represented by the 2D plane stress model shown in Fig. 10(a). It has a 1 m thickness and the material is characterized by the same CDP parameters given earlier. The model consists of a uniform mesh of CPS6M triangular elements and two-stage analysis is performed in Abaqus/CAE Explicit. The gravitational load is applied during the first 4 s followed by a rightward ground acceleration linearly increasing from 0g to 0.8g in the following 6 s. The evolution of elastic strain energy (SE), plastic dissipation energy (PD), and vertical and horizontal reactions versus analytical time is shown in Fig. 10(b). As indicated by the sharp decrease of both reactions and the simultaneous asymptotic growth of PD, failure conditions are reached at 9.23 s, which corresponds to a lateral acceleration of 0.7g.

The evolution of the damage pattern from pre- to post-failure time is shown in terms of maximum principal plastic strains in Fig. 10 (c). Grey bands denote areas where strains are in excess of 10^{-3} and are interpreted to represent actual fractures in the adobe continuum. Thus, the inertial body forces cause a shearing fracture at the base immediately followed by a secondary diagonal fracture. In kinematic terms, failure begins with the block separating from the support and sliding to the right, and it finishes with the moving block splitting diagonally and the upper triangle sliding downward.

Returning to the energy plots in Fig. 10(b), it can be noticed that SE peaks around 9.23 s, suggesting that failure time may be associated with the intersection of the PD and SE curves. Since elastic strains will actually decrease during fracture growth, it is to be expected that, at approaching failure conditions, SE will sharply decrease in the presence of total failure – as in Fig. 10(b) – or continue to grow at a lower rate for a failure involving only a portion of the structure. Thus, since in no case SE will exhibit the same asymptotic behaviour of PD, the two curves can be expected to intersect in close proximity to failure, and this condition can be effectively used to determine failure time. Furthermore, the sharp vertical asymptotic behaviour of PD at failure suggests that even considering failure conditions to correspond to PD reaching a value greater than SE would not alter the results in a meaningful way since this would only marginally increase the calculated time of failure and thus the lateral capacity. In conclusion, the geometrical condition PD = SE provides a practical and reliable way to identify the time of failure even in those cases when reactions may not be easily computed from the numerical model.

The failure determination process described above can be generalized as follows. Two stages are involved: (1) gravitational loads

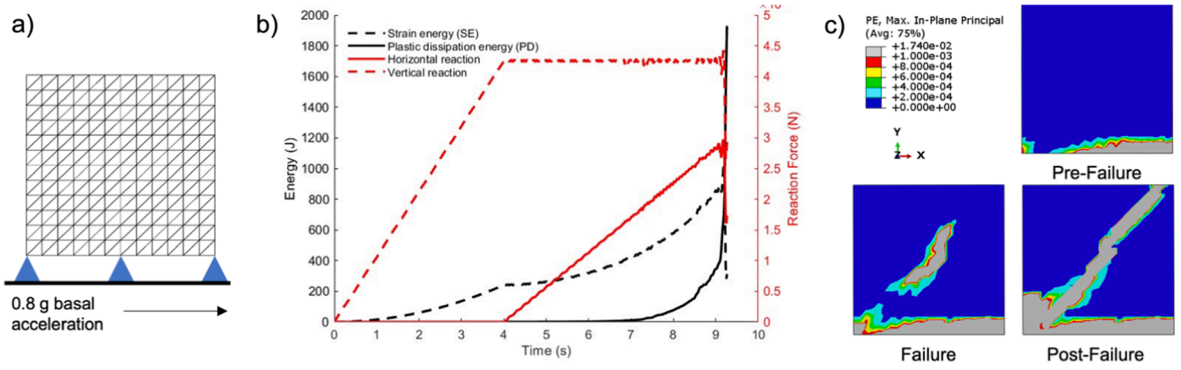

Fig. 10. Single macroblock benchmark for energy-based evaluation of failure condition and lateral capacity.

are applied with the model held in static conditions followed by (2) a pre-set lateral acceleration is applied to the boundary with the model now responding under dynamic conditions.

Stage 1: The time evolution of internal energy is monitored during gravitational loading, as some level of PD could develop depending on material properties, model geometry, and boundary conditions. If PD becomes asymptotic indicating structural collapse before static equilibrium is achieved, the analysis is halted. If PD remains lower than SE until the end of stage 1, static equilibrium is reached and the analysis can now proceed to stage 2.

Stage 2: The boundary conditions – fixed during stage 1 – are selectively released to allow a horizontal acceleration to be applied to the boundary nodes as a linear ramp increasing from zero to a pre-set value. As in the previous stage, the evolution of internal energy is monitored and the analysis is halted when PD matches SE. In case this doesn't happen within the range of applied acceleration the pre-set ramp value for Stage 2 is increased, and the entire analysis is repeated. The horizontal acceleration which produces failure conditions (i.e., PD = SE) represents the lateral capacity of the structure.

5. Sensitivity analysis

The sensitivity analysis consists of 25 models that are used to investigate the influence of the friction coefficient and the number of macroblocks on the lateral capacity and damage map obtained from each simulation. Friction coefficients range from $\mu = 0.1$ to $\mu = 0.5$, and the numbers of macroblocks discretizing the active region are 37, 56, 70, 90, and 103, as shown in configurations 1–5, Fig. 6b-f. Hereafter, each individual model is denoted by its N-μ combination. Each model was analysed using the two-stage procedure described earlier.

5.1. Illustrative example of lateral capacity estimation

The application of the energy-based methodology to the 2D macroblock model is illustrated with configuration 3 from Fig. 10 (N = 70 macroblocks) and frictional contact is defined with the coefficient $\mu = 0.3$. Based on its N-μ values, this model is labelled **70–*0.3***. Following the two-stage analysis procedure defined earlier, the model is subjected to gravitational loading over the first 5 s followed by eastward ground acceleration reaching 0.306g over the next 5 s. Fig. 11(a) shows the time evolution of the SE and PD curves produced by the eastward ground acceleration, while Fig. 11(b) gives the lateral capacity in terms of the applied ground acceleration versus horizontal displacement of representative point **P**. Plastic dissipation begins to grow at 6 s reaching 10% of SE at 7 s, turns sharply upward thereafter, and intersects strain energy at 8.11 s. This corresponds to an eastward lateral acceleration of 0.19g. The comparison with the energy plot for the benchmark problem in Fig. 10(b) gives insights into the failure process associated with the present 2D model. In the benchmark case SE peaks at the point of intersection with PD and decreases sharply thereafter, a clear indication that failure involves the totality of the structure, as confirmed by the failure pattern illustrated in Fig. 10(c). In contrast, as shown in Fig. 11

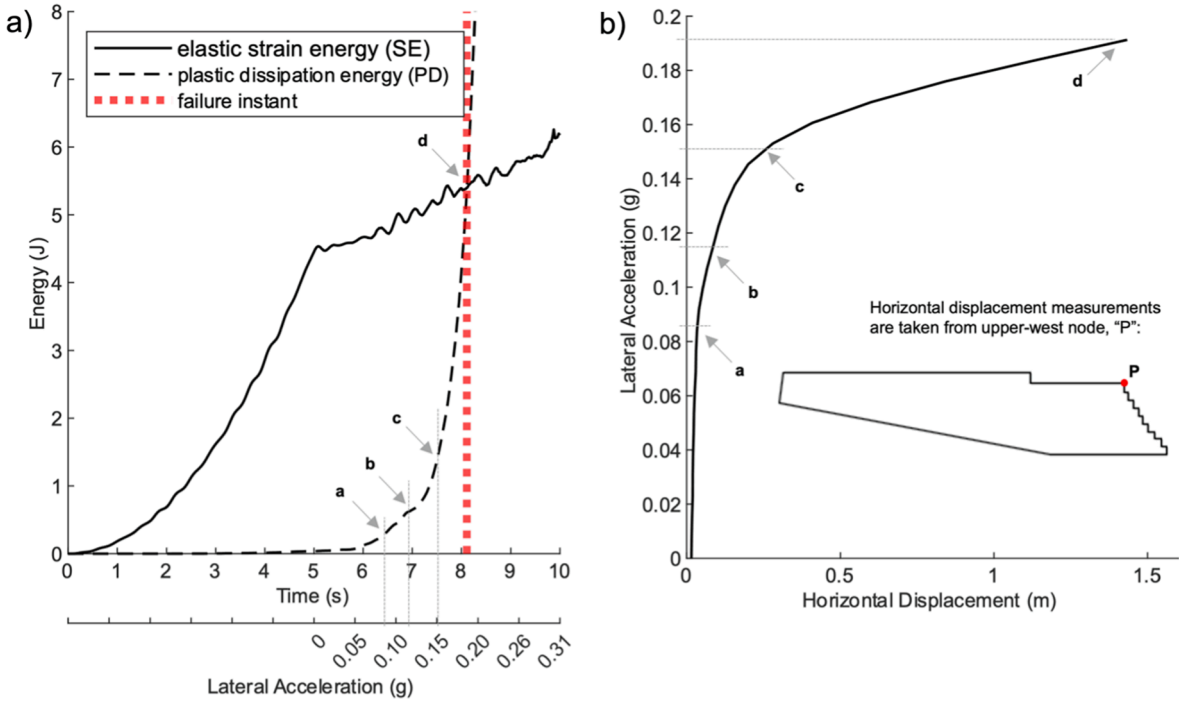

Fig. 11. Model **70–*03***: (a) Time-evolution of plastic dissipation and elastic strain energies - vertical line highlights failure instant; and (b) corresponding capacity curve in terms of applied ground acceleration versus horizontal displacement for representative point **P**.

(a) for model **70–*0.3*,** while PD becomes vertically asymptotic immediately past 8.11 s, strain energy does not peak at the same time indicating that the detected structural failure involves only a small section of the model. This is confirmed by the displacement and plastic strains patters illustrated in Fig. 12 (c-d).

The correlation between the lateral capacity curve for point P – Fig. 11(b) – and the corresponding energy plot – Fig. 11(a) – further illustrates the structural response to linearly increasing ground acceleration. The softening effect due to progressing plastic damage is clearly visible. The response is linear up to 0.08 g and increasingly softens thereafter becoming sharply plastic at 0.15 g, which corresponds to plastic dissipation reaching 25% of strain energy. As expected, since both applied acceleration and horizontal displacement at P increase monotonically throughout the analysis, the curve flattens but its slope remains positive up to failure.

The deformation and maximum principal plastic strain configurations at t = 5 s (end of gravitational loading) and t = 8.11 s (structural failure) are given in Fig. 12. The static results of macroblock model **70–*0.3*** (Fig. 12a-b) are consistent with those of the corresponding continuum pyramid models (which use the same bedrock geometry and adobe tensile strength) [54,55,57]. In both cases, the soft soil support causes a substantial increase of vertical displacements in proximity to the west façade. However, the model registers only marginal damage limited to the façade and concentrated along the steps.

The deformation and damage picture changes dramatically under dynamic conditions. At failure, the macroblocks in the upper part of the west façade begin to slide downward – Fig. 12(c). Extensive damage registers along the entire façade and large, deep fissures extend downward from the top of the model, almost splitting the structure at the point where it projects from the bedrock onto the soft soil – Fig. 12(d). The deformation and fracture patterns from this dynamic stage are also consistent with those observed from the continuum models [54,55,57]. The lateral capacity of model **70–*03*** under eastward ground acceleration is 0.19g. This finding fits within the range of 0.135g-0.34g capacity determined by the systematic analysis of 2D plane strain continuum models. The analysis of these continuum models consistently shows that westward ground acceleration produces failure conditions at higher acceleration values. Thus, the present study is limited to examining the eastward case only.

5.2. *Influence of the friction coefficient on the failure mechanism*

The effect of the friction coefficient adopted for the contact interfaces between macroblocks is illustrated with a series of five models (model **70–*0.1*** to **70–*0.5***) in which the number of macroblocks is held constant at N = 70 blocks, and the coefficient is varied from 0.1 to 0.5. The calculated lateral capacity is linearly dependent on the frictional coefficient. Values range from 0.11g to 0.24g (Δ = 118%) with **70–*0.1*** yielding the lowest value. Fig. 13 depicts the maximum principal plastic strain maps for each model, at the same lateral acceleration of a = 0.11 g (the maximum lateral acceleration for **70–*0.1***) to guarantee consistency. A significant reduction of the plastic strains and thus lower levels of expected damage in the active region are observed in **70–*0.2*** through **70–*0.5***. Damage along the façade is sharply reduced for models with higher frictional coefficients, however a deep vertical fracture originating at the re-entrant corner at the top of the pyramid is present in all the models.

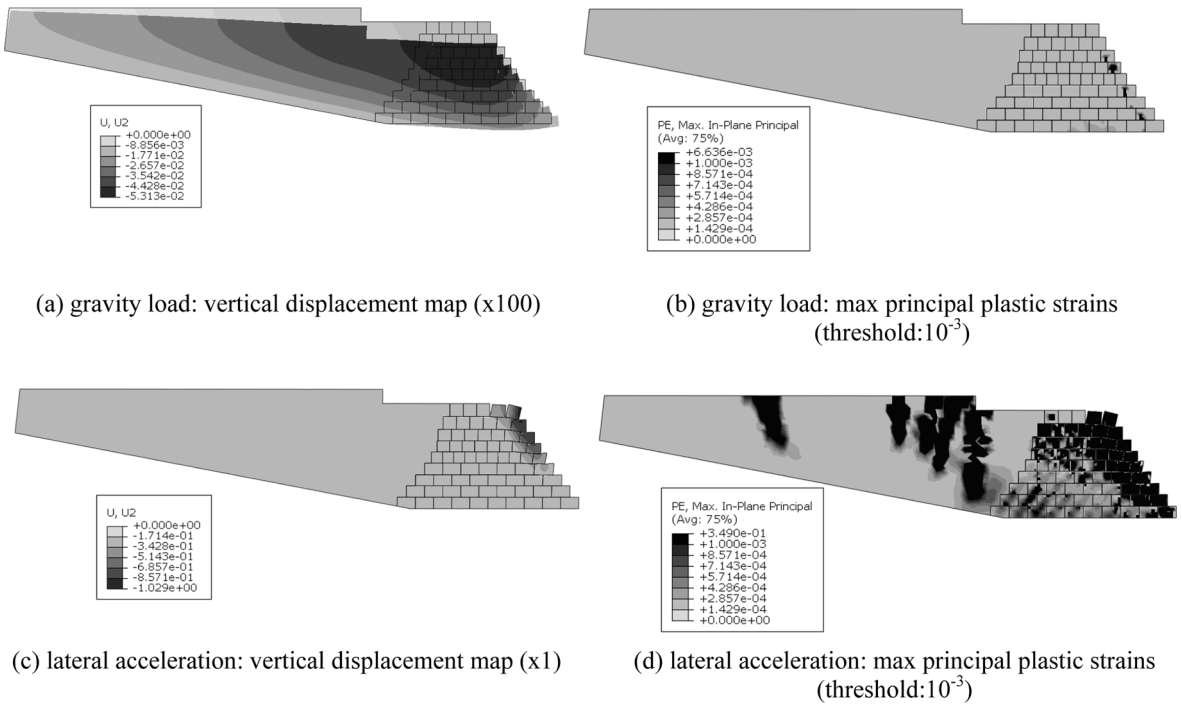

(a) gravity load: vertical displacement map (x100)

(b) gravity load: max principal plastic strains (threshold:10^{-3})

(c) lateral acceleration: vertical displacement map (x1)

(d) lateral acceleration: max principal plastic strains (threshold:10^{-3})

Fig. 12. Results after the application of the gravity (a, b) and lateral acceleration load (c, d). Maximum plastic strain maps have a threshold of 0.001.

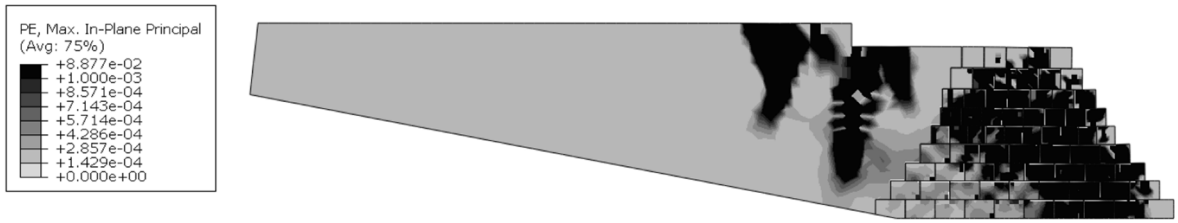

(a) Model **70-*0.1*** at a = 0.11g

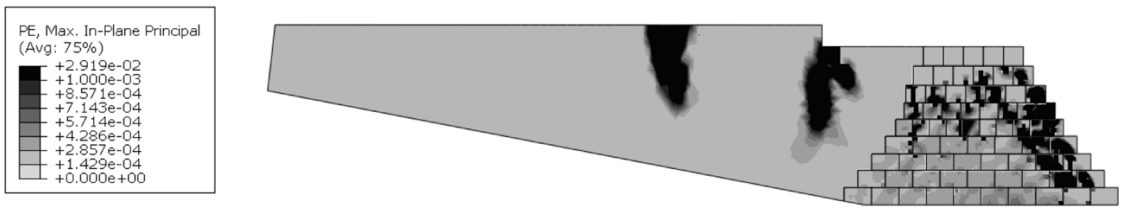

b) Model **70-*0.2*** at a = 0.11g

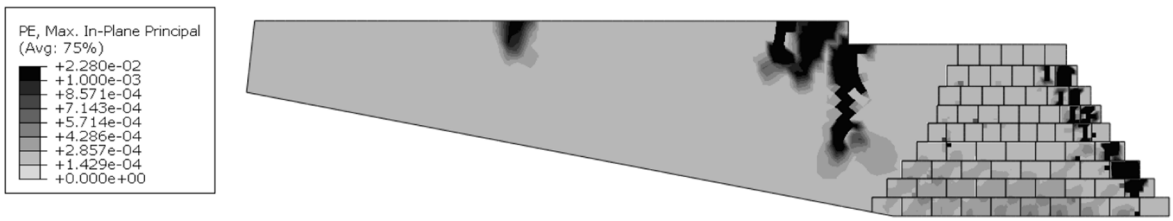

c) Model **70-*0.3*** at a = 0.11g

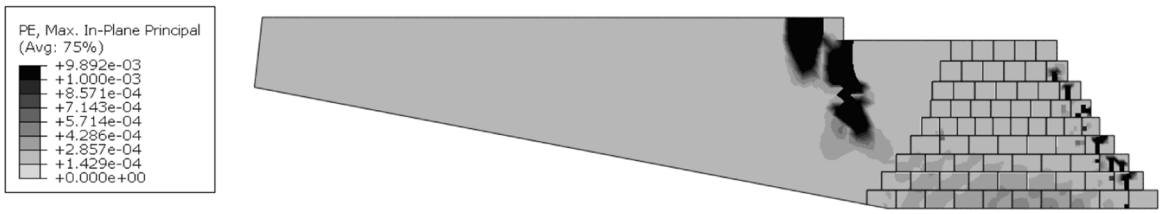

d) Model **70-*0.4*** at a = 0.11g

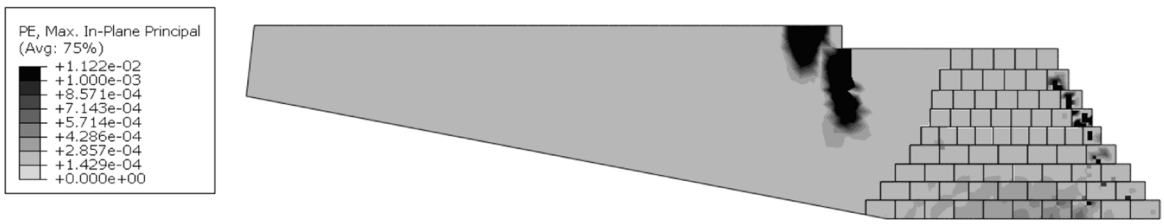

e) Model **70-*0.5*** at a = 0.11g

Fig. 13. Effect of contact friction coefficient on maximum plastic strain propagation (model 3).

5.3. Influence of the number of macroblocks on the failure mechanism

The effect of the number N of macroblocks is illustrated next. In this case, the friction coefficient is kept fixed at $\mu = 0.3$ while the numbers of macroblocks vary from N = 37 to N = 103 (models **37–*0.3*, 56–*0.3*, 70–*0.3*, 90–*0.3*,** and **103–*0.3***). The calculated lateral capacity ranges from 0.18g to 0.20g ($\Delta = 11\%$) with **90–*0.3*** yielding the lowest value. For objective comparison between models, the

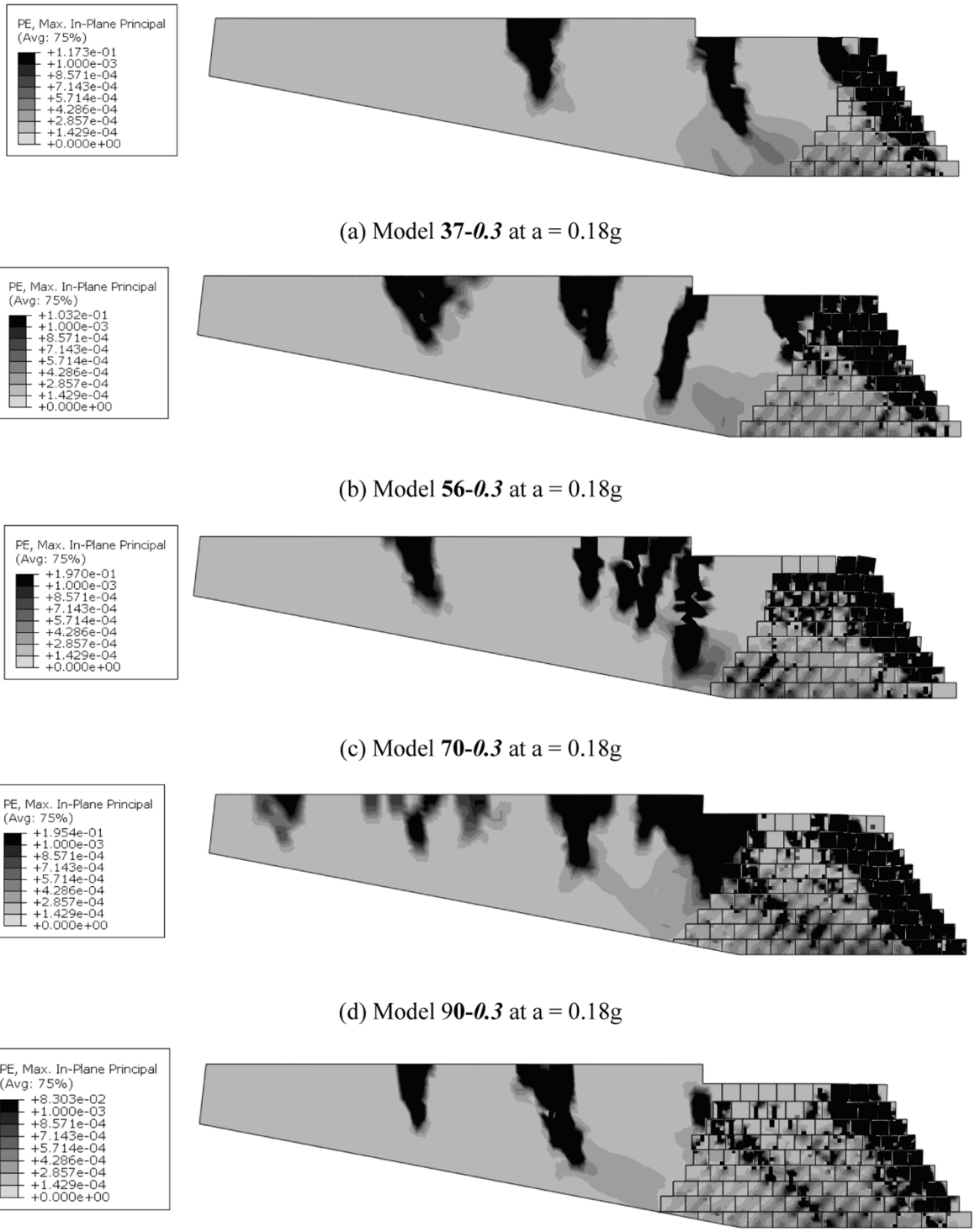

Fig. 14. Effect of the number of macroblocks on maximum plastic strain propagation ($\mu = 0.3$).

principal plastic strain maps are evaluated for each model under the same applied lateral acceleration of $a = 0.18g$ (the lowest lateral capacity from model **90**–***0.3***). Results shown in Fig. 14 indicate similar patterns of extensive damage which affect the entire façade. All models are close to failure by sliding collapse of a large triangular sector of the façade and several large vertical fractures are shown penetrating vertically from the top. Models **37**–***0.3,*** **56**–***0.3,*** **70**–***0.3,*** and **90**–***0.3*** are also characterized by a deep vertical fracture originating at the re-entrant corner and propagating in the continuum, nearly splitting the model. The same fracture appears to be deviated diagonally and substantially mitigated in model **103**–***0.3***, likely due to the presence of the blocks in this critical area. In contrast to the effect of varying the friction coefficient, increasing the number of macroblocks is found to have only a marginal effect on lateral capacity.

This point is further illustrated by comparing the energy plots for models **37**–***0.3*** and **103**–***0.3*** (Fig. 15, in blue and green). The plastic dissipation curves are in this case nearly identical, proving that the two models not only fail at the same time but also follow similar damage growth patterns up to failure. Comparing the energy plots for **70**–***0.1*** and **70**–***0.5*** **(**Fig. 15, in red and black) clearly demonstrates the difference in lateral response for the same macroblock geometry when the friction coefficient is changed from minimum to maximum. In this case, the plastic dissipation curves not only intersect the strain energy curve at two sharply separated points but also show different damage growth patterns.

5.4. Results of sensitivity analysis

The results for the complete sensitivity analysis of the lateral capacity as a function of the number of macroblocks and the coefficient of friction are reported in Table 3 and Fig. 16. Results clearly show the dominant effect of the coefficient of friction on lateral capacity, and, at the same time, the marginal effect of the number of macroblocks on each μ set. As expected, the capacity increases with the coefficient of friction. The $\Delta_{\mathbf{N}}$ and $\Delta\mu$ parameters indicate the maximum percent variation in lateral capacity for a given value of μ or N, respectively. While $\Delta_{\mathbf{N}}$ ranges between 5% and 13%, Δ_{μ} varies between 118% and 115%. The order of magnitude difference between Δ_{μ} and $\Delta_{\mathbf{N}}$ proves the dominant effect of μ versus N. The median value grows from 0.1g for $\mu = 0.1$ to 0.24g for $\mu = 0.5$, while the standard deviation does not exceed 0.01g. Taken together, these results show that for the five distributions of macroblocks considered, the coefficient of friction affects the global response (structural failure) while – as illustrated in Fig. 14 – the number of blocks alters the distribution of local damage (the evolution of internal fractures) but only marginally affects the structural failure mechanism.

5.5. Influence of the soil deformability on the lateral capacity

The relative effect of the soil foundation stiffness on the lateral capacity is also investigated. The geotechnical tests from which the average soil stiffness of E = 57 MPa was derived were conducted in front of the pyramid's north façade [64,67,69]. The actual soil stratification under the midsection of the pyramid has not been explored. To examine the effect of a stiffer support condition, the same 2D plane strain sensitivity analysis was repeated with a soil stiffness of E = 123 MPa (the adobe stiffness). The results are presented in Table 4 and show a similar pattern to those in Table 3. The coefficient of friction has a dominant effect on lateral capacity, while the effect of the number of macroblocks on each μ set remains secondary. The median values of lateral capacity increase with respect to the previous analyses (by 30% in the case of $\mu = 0.1$).

6. Conclusions and future work

A 2D nonlinear FE model was developed to explore how the Moche pier construction process used in Huaca de la Luna's main pyramid might affect the static and dynamic response to gravitational and lateral ground acceleration loading. To this end, a multi-scale approach is introduced in combination with a macro-modelling representation of adobe material. Piers of adobe bricks are modelled as macroblocks separated by frictional interfaces. The model's "active" region, identified from previous structural studies, is discretized into macroblocks and the remaining portion of the model is treated as a continuum. The analysis is conducted in Abaqus/CAE Explicit using concrete damaged plasticity and Mohr-Coulomb formulations for adobe construction and soft soil, respectively. A two-stage assessment procedure begins with a quasi-static analysis to predict the stress state due to gravitational loading. A dynamic analysis follows to identify lateral capacity and failure mechanisms triggered by monotonically increasing ground acceleration. The development of local damage conditions up to structural collapse is visualized by the nucleation and propagation of maximum principal plastic strains throughout the model.

The model geometry is based on the EW mid-section of the main pyramid introduced in earlier studies. Systematic nonlinear FE static and dynamic analysis of 2D continuum models have identified critical damage development in the western portion of the cross section, culminating with partial or total collapse of the west façade [54,55,57]. This so-called active region corresponds – within the approximation intrinsic to a 2D plane strain model – to the west façade, including the damaged NW corner of the actual pyramid. Thus, to effectively model how piers affect damage development and collapse mechanisms, macroblocks are distributed from the west façade to the interior of the cross section. Five cross sectional configurations of increasingly deep macroblock distributions are considered, with the total number of macroblocks gradually increasing from 37 to 103. Five frictional coefficients are also considered for each configuration of macroblocks, ranging from 0.1 to 0.5. Thus, a set of 25 unique nonlinear FE models are produced.

Results clearly show the dominant effect of the coefficient of friction on lateral capacity; the effect of the number of macroblocks on lateral capacity is marginal. The capacity increases with the coefficient of friction. Median values of calculated lateral capacities vary from 0.1g to 0.24g for the range of frictional factors considered. Lateral capacities given by the macroblock models are on the lower

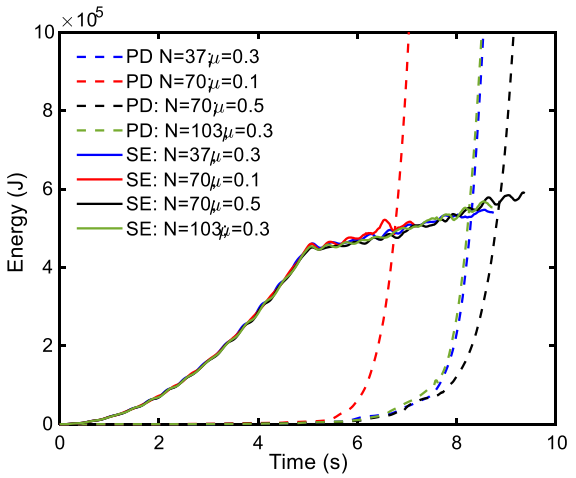

Fig. 15. Time-evolution of plastic dissipation (PD) and elastic strain energy (SE) for selected models.

Table 3
Model lateral capacity (E_{soil} = 57 MPa).

Friction coefficient (μ)	Number of macroblocks (N)							
	37	**56**	**70**	**90**	**103**	**Δ_N (%)**	**median**	**std dev**
0.1	0.10 g	0.10 g	0.11 g	0.10 g	0.10 g	**10**	**0.10 g**	0.00 g
0.2	0.17 g	0.15 g	0.16 g	0.15 g	0.16 g	**13**	**0.16 g**	0.01 g
0.3	0.20 g	0.20 g	0.19 g	0.18 g	0.20 g	**11**	**0.20 g**	0.01 g
0.4	0.21 g	0.21 g	0.21 g	0.22 g	0.21 g	**5**	**0.21 g**	0.00 g
0.5	0.23 g	0.23 g	0.24 g	0.24 g	0.25 g	**9**	**0.24 g**	0.01 g
Δ_μ (%)	**130**	**130**	**118**	**140**	**150**			

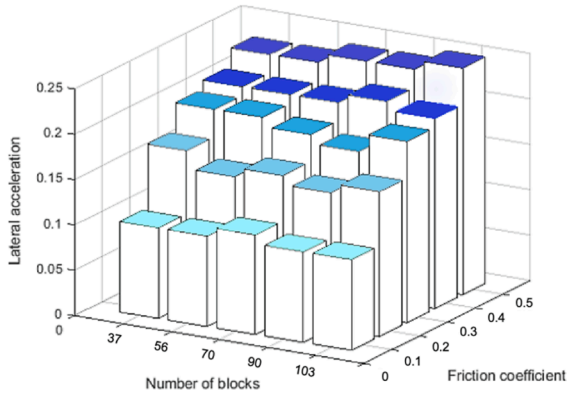

Fig. 16. Visualization of sensitivity analysis results given in Table 3 (lateral acceleration in terms of g).

Table 4
Model lateral capacity (E_{soil} = 123 MPa).

Friction coefficient (μ)	Number of macroblocks (N)							
	37	**56**	**70**	**90**	**103**	**Δ_N (%)**	**median**	**std dev**
0.1	0.13 g	0.13 g	0.13 g	0.13 g	0.13 g	**0**	**0.13 g**	0.00 g
0.2	0.17 g	0.18 g	0.14 g	0.16 g	0.17 g	**29**	**0.17 g**	0.02 g
0.3	0.22 g	0.21 g	0.23 g	0.19 g	0.22 g	**21**	**0.22 g**	0.02 g
0.4	0.22 g	0.23 g	0.23 g	0.23 g	0.23 g	**5**	**0.23 g**	0.00 g
0.5	0.26 g	0.26 g	0.26 g	0.25 g	0.25 g	**4**	**0.26 g**	0.01 g
Δ_m (%)	**100**	**100**	**100**	**92**	**92**			

end of the 0.135g-0.34g range that is calculated from 2D continuum models [54,55,57]. This range is produced by a variety of configurations that are explored via a sensitivity analysis of material, bedrock, and architectural configurations. The directly comparable continuum model from this range yields a lateral capacity of 0.34g. Assuming a coefficient of friction of 0.3 as a conservative estimate for adobe-on-adobe contact based on data in [80], the present macroblock model predicts a median lateral capacity of 0.2g. According to this estimate of the frictional coefficient, the pier architecture presently modelled with macroblocks lowers the lateral capacity by 40%. All models fail by structural collapse of the west façade and with internal damage distribution partially affected by the number of macroblocks. A qualitative survey of results shows localized plastic strains (fracture) at the west façade and on the top of the pyramid that are consistent with 2D continuum models and with extant damage.

Future research will investigate the effect of macroblock discretization with variably sized macroblocks and irregular configurations, which more closely reflects archaeological findings on the internal layered structure of the pyramid. Following the work in [54,55,57], the modelling will be extended from 2D to 3D, to more accurately represent the complex structural behaviour the actual pyramid. Finally, a time history analysis will be applied to macroblock models to evaluate the seismic vulnerability of the monument. This work also confirms the utility of an energy-based failure criterion for the assessment of the lateral capacity of structures modelled with the CDP formulation. Finally, the multi-scale approach introduced here may find application to a class of similarly built Moche earthen structures in northern Peru.

CRediT authorship contribution statement

Cristiana Riccio: Investigation, Writing – original draft, Visualization. **Anna Remus:** Validation, Data curation, Writing – review & editing. **Selman Tezcan:** Methodology, Software. **Luis C. Silva:** Visualization, Writing – original draft. **Gabriele Milani:** Conceptualization, Methodology. **Renato Perucchio:** Supervision, Methodology, Writing – review & editing.

Declaration of Competing Interest

The authors declare that they have no known competing financial interests or personal relationships that could have appeared to influence the work reported in this paper.

Data availability

Data will be made available on request.

Acknowledgments

We gratefully acknowledge the contribution of Rafael Aguilar to the discussion of pier structure of Huaca de la Luna. The last author would like to dedicate the paper to the memory of Santiago Uceda.

Co-Authors Consent

The authors confirm that the manuscript has been read and approved by all named authors. We further confirm that the order of names listed in the manuscript has been approved by all authors and that we are aware of the referred submission process.

References

[1] B.M. Feilden, Conservation of historic buildings, 3. ed., repr, Elsevier [u.a.], Amsterdam, 2005.
[2] The Venice Charter, 1994.
[3] D. Watt, Surveying Historic Buildings, 2nd ed., 2011. https://www.routledge.com/Surveying-Historic-Buildings/Watt/p/book/9781873394670 (accessed March 17, 2023).
[4] P. Roca, The study and restoration of historical structures: From principles to practice., in: P.B. Lourenco, P. Roca, S.A. Modena (Eds.), Struct. Anal. Hist. Constr., Macmillan Advanced Research Series, New Delhi, 2006: pp. 9–24.
[5] L.J. Castillo, S. Uceda, The Mochicas, in: H. Silverman, W.H. Isbell (Eds.), Handb. South Am. Archaeol., Springer, New York, 2008: pp. 707–729.
[6] S. Uceda, R. Morales, Moche: Pasado y presente, Patronato del Valle de Moche, Trujillo, Peru, 2010.
[7] A. Preciado, F. Peña, F. Colmenero Fonseca, C. Silva, Damage description and schematic crack propagation in Colonial Churches and old masonry buildings by the 2017 Puebla-Morelos earthquakes (Mw = 8.2 and 7.1), Eng. Fail. Anal. 141 (2022), 106706, https://doi.org/10.1016/j.engfailanal.2022.106706.
[8] B. Sayin, B. Yildizlar, C. Akcay, B. Gunes, The retrofitting of historical masonry buildings with insufficient seismic resistance using conventional and non-conventional techniques, Eng. Fail. Anal. 97 (2019) 454–463, https://doi.org/10.1016/j.engfailanal.2019.01.031.
[9] E. Verstrynge, L. Schueremans, D. Van Gemert, M.A.N. Hendriks, Modelling and analysis of time-dependent behaviour of historical masonry under high stress levels, Eng. Struct. 33 (2011) 210–217, https://doi.org/10.1016/j.engstruct.2010.10.010.
[10] G. Vlachakis, E. Vlachaki, P.B. Lourenço, Learning from failure: Damage and failure of masonry structures, after the 2017 Lesvos earthquake (Greece), Eng. Fail. Anal. 117 (2020), 104803, https://doi.org/10.1016/j.engfailanal.2020.104803.
[11] S. Lagomarsino, On the vulnerability assessment of monumental buildings, Bull. Earthq. Eng. 4 (2006) 445–463, https://doi.org/10.1007/s10518-006-9025-y.
[12] M. Malcata, M. Ponte, S. Tiberti, R. Bento, G. Milani, Failure analysis of a Portuguese cultural heritage masterpiece: Bonet building in Sintra, Eng. Fail. Anal. 115 (2020), 104636, https://doi.org/10.1016/j.engfailanal.2020.104636.
[13] M. Bruneau, Seismic evaluation of unreinforced masonry buildings, Can. J. Civ. Eng. 21 (1994) 512–539.
[14] M. Valente, Seismic behavior and damage assessment of two historical fortified masonry palaces with corner towers, Eng. Fail. Anal. 134 (2022), 106003, https://doi.org/10.1016/j.engfailanal.2021.106003.

[15] R. Cardoso, M. Lopes, R. Bento, Seismic evaluation of old masonry buildings. Part I: Method description and application to a case-study, Eng. Struct. 27 (2005) 2024–2035, https://doi.org/10.1016/j.engstruct.2005.06.012.
[16] G. Milani, A. Cecchi, Compatible model for herringbone bond masonry: Linear elastic homogenization, failure surfaces and structural implementation, Int. J. Solids Struct. 50 (2013) 3274–3296, https://doi.org/10.1016/j.ijsolstr.2013.05.032.
[17] M.F. Funari, A. Mehrotra, P.B. Lourenço, A Tool for the Rapid Seismic Assessment of Historic Masonry Structures Based on Limit Analysis Optimisation and Rocking Dynamics, Appl. Sci. 11 (2021) 942, https://doi.org/10.3390/app11030942.
[18] M. Valente, G. Milani, Seismic response and damage patterns of masonry churches: Seven case studies in Ferrara, Italy, Eng. Struct. 177 (2018) 809–835, https://doi.org/10.1016/j.engstruct.2018.08.071.
[19] G. Milani, M. Valente, Failure analysis of seven masonry churches severely damaged during the 2012 Emilia-Romagna (Italy) earthquake: Non-linear dynamic analyses vs conventional static approaches, Eng. Fail. Anal. 54 (2015) 13–56. https://doi.org/10.1016/j.engfailanal.2015.03.016.
[20] L. Binda, A. Saisi, C. Tiraboschi, Investigation procedures for the diagnosis of historic masonries, Constr. Build. Mater. 14 (2000) 199–233, https://doi.org/10.1016/S0950-0618(00)00018-0.
[21] G. Croci, The conservation and structural restoration of architectural heritage, Computational Mechanics Publications, Southampton, UK, 1998.
[22] ICOMOS, Recommendations for the Analysis, Conservation and Structural Restoration of Architectural Heritage, 2003.
[23] A.M. D'Altri, V. Sarhosis, G. Milani, J. Rots, S. Cattari, S. Lagomarsino, E. Sacco, A. Tralli, G. Castellazzi, S. de Miranda, Modeling Strategies for the Computational Analysis of Unreinforced Masonry Structures: Review and Classification, Arch. Comput. Methods Eng. 27 (2020) 1153–1185, https://doi.org/10.1007/s11831-019-09351-x.
[24] T.M. Ferreira, A.A. Costa, R. Vicente, H. Varum, A simplified four-branch model for the analytical study of the out-of-plane performance of regular stone URM walls, Eng. Struct. 83 (2015) 140–153, https://doi.org/10.1016/j.engstruct.2014.10.048.
[25] G. Milani, M. Valente, M. Fagone, T. Rotunno, C. Alessandri, Advanced non-linear numerical modeling of masonry groin vaults of major historical importance: St John Hospital case study in Jerusalem, Eng. Struct. 194 (2019) 458–476, https://doi.org/10.1016/j.engstruct.2019.05.021.
[26] A. Orduña Bustamante, Seismic assessment of ancient masonry structures by rigid blocks limit analysis, 2003.
[27] A. Aşıkoğlu, Ö. Avşar, P.B. Lourenço, L.C. Silva, Effectiveness of seismic retrofitting of a historical masonry structure: Kütahya Kurşunlu Mosque, Turkey, Bull. Earthq. Eng. 17 (2019) 3365–3395, https://doi.org/10.1007/s10518-019-00603-6.
[28] G. Fortunato, M.F. Funari, P. Lonetti, Survey and seismic vulnerability assessment of the Baptistery of San Giovanni in Tumba (Italy), J. Cult. Herit. 26 (2017) 64–78, https://doi.org/10.1016/j.culher.2017.01.010.
[29] M. Orlando, G. Becattini, M. Betti, Multilevel structural evaluation and rehabilitation design of an historic masonry fortress, J. Build. Eng. 63 (2023), 105379, https://doi.org/10.1016/j.jobe.2022.105379.
[30] M. Orlando, M. Betti, P. Spinelli, Assessment of structural behaviour and seismic retrofitting for an Italian monumental masonry building, J. Build. Eng. 29 (2020), 101115, https://doi.org/10.1016/j.jobe.2019.101115.
[31] T.T. Bui, A. Limam, V. Sarhosis, M. Hjiaj, Discrete element modelling of the in-plane and out-of-plane behaviour of dry-joint masonry wall constructions, Eng. Struct. 136 (2017) 277–294, https://doi.org/10.1016/j.engstruct.2017.01.020.
[32] S. Gonen, B. Pulatsu, E. Erdogmus, E. Karaesmen, E. Karaesmen, Quasi-Static Nonlinear Seismic Assessment of a Fourth Century A.D. Roman Aqueduct in Istanbul, Turkey, Heritage. 4 (2021) 401–421, https://doi.org/10.3390/heritage4010025.
[33] J. Lemos, Discrete Element Modeling of the Seismic Behavior of Masonry Construction, Buildings. 9 (2019) 43, https://doi.org/10.3390/buildings9020043.
[34] J.V. Lemos, Discrete Element Modeling of Masonry Structures, Int. J. Archit. Herit. 1 (2007) 190–213, https://doi.org/10.1080/15583050601176868.
[35] N. Savalle, É. Vincens, S. Hans, Experimental and numerical studies on scaled-down dry-joint retaining walls: Pseudo-static approach to quantify the resistance of a dry-joint brick retaining wall, Bull. Earthq. Eng. 18 (2020) 607–608, https://doi.org/10.1007/s10518-019-00702-4.
[36] M. Schiavoni, E. Giordano, F. Roscini, F. Clementi, Numerical Assessment of Interacting Structural Units on the Seismic Damage: A Comparative Analysis with Different Modeling Approaches, Appl. Sci. 13 (2023) 972, https://doi.org/10.3390/app13020972.
[37] M. Schiavoni, E. Giordano, F. Roscini, F. Clementi, Advanced numerical insights for an effective seismic assessment of historical masonry aggregates, Eng. Struct. 285 (2023), 115997, https://doi.org/10.1016/j.engstruct.2023.115997.
[38] Abaqus CAE/Explicit, 2022.
[39] A. Formisano, G. Di Lorenzo, L. Krstevska, R. Landolfo, Fem Model Calibration of Experimental Environmental Vibration Tests on Two Churches Hit by L'Aquila Earthquake, Int. J. Archit. Herit. 15 (2021) 113–131, https://doi.org/10.1080/15583058.2020.1719233.
[40] P.B. Lourenço, J. Rots, Multisurface Interface Model for Analysis of Masonry Structures, J. Eng. Mech. (1997) 660–668.
[41] S. Pietruszczak, R. Ushaksaraei, Description of inelastic behaviour of structural masonry, Int. J. Solids Struct. 40 (2003) 4003–4019, https://doi.org/10.1016/S0020-7683(03)00174-4.
[42] P.B. Lourenço, J. Rots, J. Blaauwendraad, Continuum Model for Masonry, J. Struct. Eng. (1998) 642–652.
[43] A.S. Araujo, P.B. Lourenco, D.V. Oliveira, J. Leite, Seismic Assessment of St James Church by Means of Pushover Analysis – Before and After the New Zealand Earthquake, Open Civ. Eng. J. 6 (2012) 160–172, https://doi.org/10.2174/1874149501206010160.
[44] M.F. Funari, L.C. Silva, E. Mousavian, P.B. Lourenço, Real-time Structural Stability of Domes through Limit Analysis: Application to St. Peter's Dome, Int. J Archit. Herit. (2021) 1–23, https://doi.org/10.1080/15583058.2021.1992539.
[45] P.B. Lourenço, K.J. Krakowiak, F.M. Fernandes, L.F. Ramos, Failure analysis of Monastery of Jerónimos, Lisbon: How to learn from sophisticated numerical models, Eng. Fail. Anal. 14 (2007) 280–300, https://doi.org/10.1016/j.engfailanal.2006.02.002.
[46] R. Marques, J.M. Pereira, P.B. Lourenço, W. Parker, M. Uno, Study of the Seismic Behavior of the "Old Municipal Chambers" Building in Christchurch, New Zealand, J. Earthq. Eng. 17 (2013) 350–377, https://doi.org/10.1080/13632469.2012.738283.
[47] M.G.D. Geers, V.G. Kouznetsova, W.A.M. Brekelmans, Multi-scale computational homogenization: Trends and challenges, J. Comput. Appl. Math. 234 (2010) 2175–2182, https://doi.org/10.1016/j.cam.2009.08.077.
[48] P.C. Gehlen, G.T. Hahn, M.F. Kanninen, Crack extension by bond rupture in a model of BCC iron, Scr. Metall. 6 (1972) 1087–1090, https://doi.org/10.1016/0036-9748(72)90193-7.
[49] J.E. Sinclair, The influence of the interatomic force law and of kinks on the propagation of brittle cracks, Philos. Mag. J. Theor. Exp. Appl. Phys. 31 (1975) 647–671, https://doi.org/10.1080/14786437508226544.
[50] M.L. De Bellis, D. Addessi, A cosserat based multi-scale model for masonry structures, J. Multiscale Comput. Eng. 9 (2011) 543–563.
[51] C. Driesen, H. Degée, B. Vandoren, Efficient modeling of masonry failure using a multiscale domain activation approach, Comput. Struct. 251 (2021), 106543, https://doi.org/10.1016/j.compstruc.2021.106543.
[52] M.F. Funari, L.C. Silva, N. Savalle, P.B. Lourenco, A concurrent micro/macro FE-model optimized with a limit analysis too for the assessment of dry-joint masonry structures, Int. J. Multiscale Comput. Eng. 20 (2022) 65–85, https://doi.org/10.1615/IntJMultCompEng.2021040212.
[53] H. Talebi, M. Silani, T. Rabczuk, Concurrent multiscale modeling of three dimensional crack and dislocation propagation, Adv. Eng. Softw. 80 (2015) 82–92, https://doi.org/10.1016/j.advengsoft.2014.09.016.
[54] S. Tezcan, Nonlinear Finite Element Static and Dynamic Analysis of the Main Pyramid of Huaca de la Luna, Peru, PhD, University of Rochester, 2022.
[55] S. Tezcan, M. a. Pando, R. Aguilar, B. Castañeda, C. Rojas, R. Perucchio, Preliminary nonlinear static and dynamic analysis of the main pyramid of Huaca de la Luna, Peru, in: M. Papadrakakis, M. Fragiadakis (Eds.), COMPDYN 2021 8th ECCOMAS Themat. Conf. Comput. Methods Struct. Dyn. Earthq. Eng., Athens, Greece, 2021: pp. 244–257. https://doi.org/10.7712/120121.8478.18791.
[56] S. Tezcan, N. Tambe, C. Muir, R. Aguilar, R. Perucchio, Nonlinear FE Analysis of the Response to Lateral Accelerations of the Triumphal Arch of the Church of Andahuaylillas, Peru, in: R. Aguilar, D. Torrealva, S. Moreira, M.A. Pando, L.F. Ramos (Eds.), Struct. Anal. Hist. Constr., Springer International Publishing, Cham, 2019: pp. 1301–1309. https://doi.org/10.1007/978-3-319-99441-3_139.
[57] S. Tezcan, M.A. Pando, R. Aguilar, R. Perucchio, Nonlinear 2D and 3D Finite Element Static and Dynamic Analysis of the Main Pyramid of Huaca de la Luna, Peru, in: IEndo, Y., Hanazato, T. (eds.) 13th Int. Conf. on Structural Analysis of Historical Constructions (SAHC 2023), Kyoto, Japan (2023).Kyoto, Japan, 2023.

[58] L. Giresini, Energy-based method for identifying vulnerable macro-elements in historic masonry churches, Bull. Earthq. Eng. 14 (2016) 919–942, https://doi.org/10.1007/s10518-015-9854-7.
[59] A. Iannuzzo, P. Block, M. Angelillo, A. Gesualdo, A continuous energy-based numerical approach to predict fracture mechanisms in masonry structures: CDF method, Comput. Struct. 257 (2021), 106645, https://doi.org/10.1016/j.compstruc.2021.106645.
[60] R. Aguilar, G. Zavala, B. Castañeda, S. Lopez, S. Retamozo, M. Montesinos, M.A. Pando, Y. Dong, R. Perucchio, Structural damage assessment of Huaca de la Luna, Perú: Preliminary results from ongoing multidisciplinary study, in: K. Van Balen, E. Verstrynge (Eds.), Struct. Anal. Hist. Constr. Anamn. Diagn. Ther. Controls, 0 ed., CRC Press, 2016: pp. 465–472. https://doi.org/10.1201/9781315616995-62.
[61] L.M. Zanchetta, M. Quattrone, R. Aguilar, H. Kahn, A.C.V. Coelho, V.M. John, Microstructures of Building Materials from Huaca De La Luna, Peru, Int. J. Archit. Herit. 14 (2020) 256–273, https://doi.org/10.1080/15583058.2018.1531181.
[62] C.M. Hastings, M.E. Moseley, The Adobes of Huaca del Sol and Huaca de La Luna, Am. Antiq. 40 (1975) 196–203, https://doi.org/10.2307/279615.
[63] M. Bridges, Planet Peru: an aerial journey through a timeless land, Professional Photography Division of Eastman Kodak Co., New York, N.Y., 1991.
[64] R. Aguilar, M.A. Pando, C. Briceño, G. Zavala, B. Castañeda, R. Perucchio, S. Uceda, Structural and geotechnical engineering assessment of Huaca de la Luna – A massive earthen Moche culture pyramid in Northern Peru, J. Cult. Herit. 34 (2018) 83–94, https://doi.org/10.1016/j.culher.2018.04.006.
[65] C. Chácara, F. Zvietcovich, R. Aguilar, R. Perucchio, R. Marques, B. Castañeda, S. Uceda, R. Morales, Preliminary structural assessment of adobe archaeological remains of " Huaca de la Luna " in Trujillo, Peru, (2014). https://doi.org/10.13140/RG.2.1.2789.4809.
[66] F. Zvietcovich, B. Castaneda, R. Perucchio, 3D solid model updating of complex ancient monumental structures based on local geometrical meshes, Digit. Appl. Archaeol. Cult. Herit. 2 (2015) 12–27, https://doi.org/10.1016/j.daach.2015.02.001.
[67] R. Aguilar, M. Montesinos, S. Uceda, Mechanical characterization of the structural components of Pre-Columbian earthen monuments: Analysis of bricks and mortar from Huaca de la Luna in Perú, Case Stud, Constr. Mater. 6 (2017) 16–28, https://doi.org/10.1016/j.cscm.2016.11.003.
[68] E. Ramírez, M. Montesinos, R. Marques, R. Morales, S. Uceda, P.B. Lourenço, R. Aguilar, Análisis mecánico de albañilería arqueológica de adobe bajo cargas de, in, University of Seville, Seville, Spain, 2015, pp. 77–90.
[69] G. Zavala, S. Lopez, M.A. Pando, J. Zegarra, R. Morales, S. Uceda, B. Castañeda, R. Aguilar, Geotechnical and geophysical exploration in archaeological heritage - initial assessment at Huaca de la Luna, in: D. Manzanal, A.O. Sfriso (Eds.), Fundam. Appl. Geotech., IOS Press, Buenos Aires, Argentina, 2015.
[70] A. Ferrante, M. Schiavoni, F. Bianconi, G. Milani, F. Clementi, Influence of Stereotomy on Discrete Approaches Applied to an Ancient Church in Muccia, Italy, J. Eng. Mech. 147 (2021) 04021103, https://doi.org/10.1061/(ASCE)EM.1943-7889.0002000.
[71] P.B. Lourenco, L.C. Silva, Computational applications in masonry structures: From the meso-scale to the super-large/super-complex, Int. J. Multiscale Comput. Eng. 18 (2020) 1–30, https://doi.org/10.1615/IntJMultCompEng.2020030889.
[72] J.M. Fages, N. Tarque, J.D. Rodríguez-Mariscal, M. Solís, Calibration of a total strain crack model for adobe masonry based on compression and diagonal compression tests, Constr. Build. Mater. 352 (2022), 128965, https://doi.org/10.1016/j.conbuildmat.2022.128965.
[73] A. Ferrante, E. Giordano, F. Clementi, G. Milani, A. Formisano, FE vs. DE Modeling for the Nonlinear Dynamics of a Historic Church in Central Italy, Geosciences. 11 (2021) 189. https://doi.org/10.3390/geosciences11050189.
[74] G.A. Cundari, G. Milani, G. Failla, Seismic vulnerability evaluation of historical masonry churches: Proposal for a general and comprehensive numerical approach to cross-check results, Eng. Fail. Anal. 82 (2017) 208–228, https://doi.org/10.1016/j.engfailanal.2017.08.013.
[75] L.C.M. da Silva, G. Milani, A FE-Based Macro-Element for the Assessment of Masonry Structures: Linear Static, Vibration, and Non-Linear Cyclic Analyses, Appl. Sci. 12 (2022) 1248, https://doi.org/10.3390/app12031248.
[76] J. Lee, G.L. Fenves, Plastic-Damage model for cyclic loading of concrete structures, J. Eng. Mech. (1998) 892–900.
[77] J. Lubliner, J. Oliver, S. Oller, E. Oñate, A plastic-damage model for concrete, Int. J. Solids Struct. 25 (1989) 299–326, https://doi.org/10.1016/0020-7683(89)90050-4.
[78] A. Sánchez, H. Varum, T. Martins, J. Fernández, Mechanical properties of adobe masonry for the rehabilitation of buildings, Constr. Build. Mater. 333 (2022), 127330, https://doi.org/10.1016/j.conbuildmat.2022.127330.
[79] F. Faleri, N. Grillanda, S. Tezcan, R. Perucchio, G. Milani, Role of repeated seismic events on the collapse of two calidaria in Rome dating back to the Imperial Age, in: Athens, Greece, 2021: pp. 406–414. https://doi.org/10.7712/120121.8494.19238.
[80] Naval Facilities Engineering Command, Foundations & Earth Structures, 1986.